Angle-resolved photoemission from crystal-field-split adatom levels

J. F. Herbst[*][†]

National Bureau of Standards, Washington, D.C. 20234

(Received 16 September 1976)

We investigate the angular distribution of photoelectrons emitted from atoms physisorbed on the surface of a metal. The crystalline electric field of the surface is represented by a small number of point charges in the vicinity of the adatom, and the splittings of p and d adatom levels in the crystal field are calculated. The spin-orbit splitting of the adatom states is assumed to be large in comparison with the crystal-field effects. For adatom p levels we consider both fourfold and bridge sites on a (100) surface of an fcc or bcc metal, and we include results for d states in the fourfold configuration. Within the dipole approximation photoelectron distributions are calculated for these cases assuming normally incident, unpolarized light. The results demonstrate that the angular distributions are sensitive to substrate geometry. Implications of this work for recent ultraviolet photoemission experiments involving xenon and mercury adsorbed on a tungsten surface are discussed.

I. INTRODUCTION

Considerable theoretical and experimental effort is currently being focused on the angle-resolved photoemission spectra of electrons emitted from adsorbate-covered surfaces. It has been shown[1,2] that analysis of angle-resolved photoemission spectra can yield significant information regarding adsorbate positions, bond geometries of chemisorbed species, orbital shapes, and the like. Physisorbed systems may be considered prototypical since the adsorbate-substrate interaction energies are roughly an order of magnitude smaller than those characterizing chemisorption. The primary feature distinguishing photoemission in these systems from gas-phase work is the specific orientation of the adsorbate on the surface.

In this paper we investigate the angular distributions for atoms physisorbed on the surface of a metal through analysis of a simple model. The interaction between the adatom and the surface is represented by a crystalline electric field generated by a small number of point charges in the neighborhood of the adsorbate. Since an adatom lies partially inside the dipole layer of the substrate, the substrate ion cores will not be totally shielded by the conduction electrons; the basic symmetry of the problem is maintained by replacing the partially screened ions with point charges. We consider p and d levels in fourfold sites, and also p levels in bridge sites, on a (100) surface of an fcc or bcc metal. The energies and wave functions of these levels in the presence of the crystal field are first calculated under the assumption that the free-atom spin-orbit splitting is large compared to the crystal-field effects (which is the case for the specific examples to be treated). The crystal field lifts some of the free-

atom degeneracies and leads to states differing in energy which, in general, are not spherically symmetric. Therefore, the angular distributions of electrons emitted from these states (provided the energy splittings are resolvable) will differ from the gas-phase results in a fashion dependent upon the substrate geometry, and we demonstrate this explicitly by calculating the distributions for normally incident, unpolarized light within the dipole approximation.

In Sec. II elementary perturbation theory is applied to find the energies and wave functions of the crystal-field levels; angular distributions are calculated in Sec. III, and we discuss the correspondence with gas-phase theory. One advantage of our approach is that the angular factors can be determined analytically. Sections IV and V deal with application of the model to the Xe-W(100) and Hg-W(100) systems for which experimental data have recently become available. Concluding remarks are given in Sec. VI.

II. CRYSTAL-FIELD ENERGIES AND PERTURBED ADATOM WAVE FUNCTIONS

For the physisorbed systems of interest here we assume an adatom to reside partly within the dipole layer formed by the outermost electron orbitals of the substrate atoms, so that in the immediate vicinity of the adsorbate the substrate ion cores are incompletely shielded. The simplest approximation which preserves the symmetry of the situation is to replace the partially screened neighboring ions by point charges. We consider fourfold and bridge sites on the (100) surface of an fcc or bcc metal. Figure 1 illustrates the configurations and coordinate axes. The origin of coordinates coincides with the adatom nucleus, which is located a distance h above
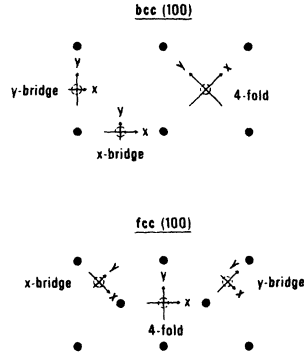
FIG. 1. Coordinate systems for adatom sites on bcc and fcc (100) surfaces. The x and y directions for the fourfold and bridge sites are indicated; the z axis points out of the paper. In each case the adatom nucleus is the origin of coordinates and is situated above the dashed circle.

the first plane of substrate ion cores. In the fourfold case five point charges are taken into account, four in the first substrate plane and one in the second plane directly below the adatom[3]; their positions (x, y, z) are $(\pm f, 0, -h)$, $(0, \pm f, -h)$, and $(0, 0, -h - \frac{1}{2}c)$, where $f = (c/\sqrt{2})$ (bcc), $f = \frac{1}{2}c$ (fcc), and c is the lattice constant of the metal. We use two nearest-neighbor point charges for bridge sites; for the x bridge their coordinates are $(\pm d, 0, -h)$ and for the y bridge $(0, \pm d, -h)$, where $d = \frac{1}{2}c$ (bcc), $d = (c/2\sqrt{2})$ (fcc).

Assuming for simplicity that all the point charges in each case are identical[4] and of strength $Z|e|$, the potential energy of an adatom electron at point $\vec{r}$ due to the crystal field is (in atomic units)

$$V = -Z \sum_i \frac{1}{|\vec{r} - \vec{R}_i|}$$

$$= -4\pi Z \sum_i \sum_{l=0,2,4} \sum_{m=-l}^{l} \frac{1}{2l+1} \frac{r^l}{R_i^{l+1}} Y_{lm}^*(\Omega_i) Y_{lm}(\Omega).$$

(1)

The subscript i refers to the point-charge positions. We have expanded V in spherical har-

monics and have retained the indicated terms since the only components of the potential which can affect p states are those with $l = 0, 2$ and d states $l = 0, 2, 4$. The potential $V^{(4)}$ for the four-fold configuration can be written

$$V^{(4)} = V_0^{(4)} + r^2 V_{20}^{(4)} Y_{20}(\Omega) + r^4 V_{40}^{(4)} Y_{40}(\Omega)$$

$$+ r^4 V_{44}^{(4)}[Y_{44}(\Omega) + Y_{4,-4}(\Omega)] ; \quad (2a)$$

the coefficients are

$$V_0^{(4)} = -(4Z/R_1 + Z/R_2) , \quad (2b)$$

$$V_{20}^{(4)} = -(\tfrac{1}{5}\pi)^{1/2}[(4Z/R_1^3)(3\cos^2\beta - 1) + 2Z/R_2^3] , \quad (2c)$$

$$V_{40}^{(4)} = -\tfrac{1}{12}(\pi)^{1/2}[(4Z/R_1^5)(35\cos^4\beta - 30\cos^2\beta + 3) + 8Z/R_2^5] , \quad (2d)$$

$$V_{44}^{(4)} = -(4Z/R_1^5)(\tfrac{35}{288}\pi)^{1/2}\sin^4\beta , \quad (2e)$$

where $R_1 = (f^2 + h^2)^{1/2}$, $R_2 = h + \frac{1}{2}c$, and $\cos\beta = -h/R_1$. Similarly, the potential $V^{(2)}$ appropriate for p electrons in the bridge configurations is

$$V^{(2)} = V_0^{(2)} + r^2 V_{20}^{(2)} Y_{20}(\Omega) + r^2 V_{22}^{(2)}[Y_{22}(\Omega) + Y_{2,-2}(\Omega)],$$

(3a)

in which

$$V_0^{(2)} = -(2Z/R) , \quad (3b)$$

$$V_{20}^{(2)} = -(2Z/R^3)(\tfrac{1}{5}\pi)^{1/2}(3\cos^2\beta - 1) , \quad (3c)$$

$$V_{22}^{(2)} = \mp(2Z/R^3)(\tfrac{3}{10}\pi)^{1/2}\sin^2\beta , \quad (3d)$$

and $R = (d^2 + h^2)^{1/2}$, $\cos\beta = -h/R$; the upper sign in Eq. (3d) pertains to the x bridge, the lower sign to the y bridge.

Elementary perturbation theory can now be applied to find the effect of V on the adatom levels. We work in the one-electron approximation and assume the spin-orbit splitting (1–2 eV for the specific examples to be treated later) to be large compared to the splitting produced by V (typically a few tenths of an eV). The unperturbed adatom wave functions are taken to be spin-orbit eigenfunctions, i.e., eigenstates[5] of the total angular momentum j and its z component m:

$$|n l j = l + \tfrac{1}{2} m\rangle = R_{nlj}(r)\left[\left(\frac{l+m+\tfrac{1}{2}}{2l+1}\right)^{1/2} Y_{l,m-\frac{1}{2}}(\Omega)|\uparrow\rangle + \left(\frac{l-m+\tfrac{1}{2}}{2l+1}\right)^{1/2} Y_{l,m+\frac{1}{2}}(\Omega)|\downarrow\rangle\right] ,$$

$$|n l j = l - \tfrac{1}{2} m\rangle = R_{nlj}(r)\left[\left(\frac{l-m+\tfrac{1}{2}}{2l+1}\right)^{1/2} Y_{l,m-\frac{1}{2}}(\Omega)|\uparrow\rangle - \left(\frac{l+m+\tfrac{1}{2}}{2l+1}\right)^{1/2} Y_{l,m+\frac{1}{2}}(\Omega)|\downarrow\rangle\right] .$$

(4)

Spin functions are denoted by $|\uparrow\rangle$ and $|\downarrow\rangle$, n is the principal quantum number, and the radial wave functions $R_{nlj}(r)$ are in general different for the two j values associated with a given orbital angular

momentum l. The first-order perturbed energies and eigenfunctions are simply found by diagonalizing the $(2j + 1)$-dimensional matrix $\langle jm|V|jm'\rangle$ for each j. Evaluation of the matrix elements is facil-

TABLE I. Perturbed energies and wave functions for adatom p levels in the fourfold site crystal field defined by $V^{(4)}$ of Eq. (2).

	Energy	Wave functions
$p_{1/2}$:	$E_1 = \epsilon_{1/2} + V_0^{(4)}$	$\lvert \tfrac{1}{2} \pm \tfrac{1}{2} \rangle$
$p_{3/2}$:	$E_2 = \epsilon_{3/2} + V_0^{(4)} + \chi$	$\lvert \tfrac{3}{2} \pm \tfrac{3}{2} \rangle$
	$E_3 = \epsilon_{3/2} + V_0^{(4)} - \chi$	$\lvert \tfrac{3}{2} \pm \tfrac{1}{2} \rangle$
	$\chi = -[1/(20\pi)^{1/2}] \langle r^2 \rangle_{3/2} V_{20}^{(4)}$	

itated by noting that the Gaunt coefficients

$$c^k(lm, l'm')$$

$$= \left(\frac{4\pi}{2k+1} \right)^{1/2} \int d\Omega \, Y_{lm}^*(\Omega) Y_{k,m-m'}(\Omega) Y_{l'm'}(\Omega) \quad (5)$$

can be found in tables.[6]

A. p states in fourfold sites

From Eqs. (4), the wave functions $\lvert jm \rangle$ for adatom p levels are

$$\lvert \tfrac{1}{2}\tfrac{1}{2} \rangle = R_{1/2}[(\tfrac{1}{3})^{1/2} Y_{10} \lvert \uparrow \rangle - (\tfrac{2}{3})^{1/2} Y_{11} \lvert \downarrow \rangle] \ ,$$

$$\lvert \tfrac{1}{2} -\tfrac{1}{2} \rangle = R_{1/2}[(\tfrac{2}{3})^{1/2} Y_{1,-1} \lvert \uparrow \rangle - (\tfrac{1}{3})^{1/2} Y_{10} \lvert \downarrow \rangle], \quad j = \tfrac{1}{2} \ ; \quad (6)$$

$$\lvert \tfrac{3}{2}\tfrac{3}{2} \rangle = R_{3/2} Y_{11} \lvert \uparrow \rangle \ ,$$

$$\lvert \tfrac{3}{2}\tfrac{1}{2} \rangle = R_{3/2}[(\tfrac{2}{3})^{1/2} Y_{10} \lvert \uparrow \rangle + (\tfrac{1}{3})^{1/2} Y_{11} \lvert \downarrow \rangle] \ ,$$

$$\lvert \tfrac{3}{2} -\tfrac{1}{2} \rangle = R_{3/2}[(\tfrac{1}{3})^{1/2} Y_{1,-1} \lvert \uparrow \rangle + (\tfrac{2}{3})^{1/2} Y_{10} \lvert \downarrow \rangle], \quad (7)$$

$$\lvert \tfrac{3}{2} -\tfrac{3}{2} \rangle = R_{3/2} Y_{1,-1} \lvert \downarrow \rangle, \quad j = \tfrac{3}{2} \ .$$

The charge density of each of the $p_{1/2}$ states is spherically symmetric (as is readily verified), so to first order they will not separate in any crystal field; the only effect of $V^{(4)}$ is to shift their energy by the constant $V_0^{(4)}$. The 4×4 matrix $\langle \tfrac{3}{2} m \lvert V^{(4)} \rvert \tfrac{3}{2} m' \rangle$ for the $p_{3/2}$ states is already diagonal in the basis set chosen here. Table I details the results; the ϵ_j are the unperturbed (i.e., free atom) one-elec-

tron energies, and $\langle r^k \rangle_j$ is the radial matrix element

$$\langle r^k \rangle_j = \int_0^\infty r^2 \, dr \, R_{nlj}^2(r) r^k \ . \quad (8)$$

$V^{(4)}$ splits the $p_{3/2}$ states into two doubly degenerate levels whose energy separation is $2\lvert \chi \rvert$.

B. p states in bridge sites

In this case the $p_{1/2}$ states are merely shifted by $V_0^{(2)}$, and the matrix $\langle \tfrac{3}{2} m \lvert V^{(2)} \rvert \tfrac{3}{2} m' \rangle$ can be cast in the form

$$\begin{pmatrix} A & 0 \\ 0 & A \end{pmatrix},$$

where A is a 2×2 matrix; the problem thus reduces to the familiar two-state exercise of elementary quantum mechanics. Results are given in Table II; the individual phases of the mixing coefficients a_1 and a_2 have been specified by arbitrarily choosing a_1 to be real and positive. The splitting of the $p_{3/2}$ levels is qualitatively the same as for the fourfold geometry, but the $V_{22}^{(2)}$ term in $V^{(2)}$ causes mixing of the unperturbed states which leads to different angular distributions for the bridge and fourfold configurations, as we shall see. Note that the splitting is the same for the x and y bridges while the sign of the mixing coefficient a_2, which depends on the sign of $V_{22}^{(2)}$ [see Eq. (3d)], is opposite in the two cases.

C. d states in fourfold sites

Wave functions for the unperturbed $d_{3/2}$ and $d_{5/2}$ states are given by Eqs. (4) with $l = 2$. Solution of the perturbation problem for the $d_{3/2}$ levels is quite similar to that for the $p_{3/2}$ states in the same geometry, and diagonalization of the 6×6 matrix $\langle \tfrac{5}{2} m \lvert V^{(4)} \rvert \tfrac{5}{2} m' \rangle$ again involves no more difficulty than the two-state problem. Table III summarizes the calculations. The initially sixfold degenerate $d_{5/2}$ states are split into three doubly degenerate levels by $V^{(4)}$.

TABLE II. Perturbed energies and wave functions for adatom p levels in the bridge site crystal field defined by $V^{(2)}$ of Eq. (3).

	Energy	Wave functions
$p_{1/2}$:	$E_1 = \epsilon_{1/2} + V_0^{(2)}$	$\lvert \tfrac{1}{2} \pm \tfrac{1}{2} \rangle$
$p_{3/2}$:	$E_2 = \epsilon_{3/2} + V_0^{(2)} + (\chi^2 + \eta^2)^{1/2}$	$a_1 \lvert \tfrac{3}{2} \pm \tfrac{3}{2} \rangle + a_2 \lvert \tfrac{3}{2} \mp \tfrac{1}{2} \rangle$
	$E_3 = \epsilon_{3/2} + V_0^{(2)} - (\chi^2 + \eta^2)^{1/2}$	$a_2 \lvert \tfrac{3}{2} \pm \tfrac{3}{2} \rangle - a_1 \lvert \tfrac{3}{2} \mp \tfrac{1}{2} \rangle$
	$\chi = -[1/(20\pi)^{1/2}] \langle r^2 \rangle_{3/2} V_{20}^{(2)}$	$\eta = -[1/(10\pi)^{1/2}] \langle r^2 \rangle_{3/2} V_{22}^{(2)}$
	$a_1 = \{\tfrac{1}{2}[1 + \chi/(\chi^2 + \eta^2)^{1/2}]\}^{1/2}$	$a_2 = (\eta/\lvert \eta \rvert)\{\tfrac{1}{2}[1 - \chi/(\chi^2 + \eta^2)^{1/2}]\}^{1/2}$

TABLE III. Perturbed energies and wave functions for adatom d levels in the fourfold site crystal field defined by $V^{(4)}$ of Eq. (2).

	Energy	Wave functions
$d_{3/2}$:	$E_1 = \epsilon_{3/2} + V_0^{(4)} + \chi$	$\lvert \frac{3}{2} \pm \frac{3}{2} \rangle$
	$E_2 = \epsilon_{3/2} + V_0^{(4)} - \chi$	$\lvert \frac{3}{2} \pm \frac{1}{2} \rangle$
	$\chi = -[1/(20\pi)^{1/2}] \langle r^2 \rangle_{3/2} V_{20}^{(4)}$	
$d_{5/2}$:	$E_3 = \epsilon_{5/2} + V_0^{(4)} + \eta_1$	$\lvert \frac{5}{2} \pm \frac{1}{2} \rangle$
	$E_4 = \epsilon_{5/2} + V_0^{(4)} + \frac{1}{2}(\eta_2 + \eta_3 + \Phi)$	$a_1 \lvert \frac{5}{2} \pm \frac{5}{2} \rangle + a_2 \lvert \frac{5}{2} \mp \frac{3}{2} \rangle$
	$E_5 = \epsilon_{5/2} + V_0^{(4)} + \frac{1}{2}(\eta_2 + \eta_3 - \Phi)$	$a_2 \lvert \frac{5}{2} \pm \frac{5}{2} \rangle - a_1 \lvert \frac{5}{2} \mp \frac{3}{2} \rangle$
	$\Phi = [(\eta_2 - \eta_3)^2 + 4\eta_4^2]^{1/2}$	
	$\eta_1 = \frac{4}{7}[1/(5\pi)^{1/2}] \langle r^2 \rangle_{5/2} V_{20}^{(4)} + [1/7(\pi)^{1/2}] \langle r^4 \rangle_{5/2} V_{40}^{(4)}$	
	$\eta_2 = -\frac{1}{7}(5/\pi)^{1/2} \langle r^2 \rangle_{5/2} V_{20}^{(4)} + [1/14(\pi)^{1/2}] \langle r^4 \rangle_{5/2} V_{40}^{(4)}$	
	$\eta_3 = \frac{1}{7}[1/(5\pi)^{1/2}] \langle r^2 \rangle_{5/2} V_{20}^{(4)} - [3/14(\pi)^{1/2}] \langle r^4 \rangle_{5/2} V_{40}^{(4)}$	
	$n_4 = [1/(14\pi)^{1/2}] \langle r^4 \rangle_{5/2} V_{44}^{(4)}$	
	$a_1 = \left[\frac{1}{2}\left(1 + \frac{\eta_2 - \eta_3}{\Phi}\right)\right]^{1/2}$	$a_2 = \frac{\eta_4}{\lvert \eta_4 \rvert}\left[\frac{1}{2}\left(1 - \frac{\eta_2 - \eta_3}{\Phi}\right)\right]^{1/2}$

III. ANGULAR DISTRIBUTIONS FOR UNPOLARIZED LIGHT AT NORMAL INCIDENCE

In the dipole approximation, which is excellent for low-energy photons, the differential cross section for photoionization of an adatom state $\lvert i \rangle$ is proportional to the absolute square of a dipole matrix element:

$$\frac{d\sigma}{d\Omega} \propto \lvert \langle fm_s \lvert \hat{\epsilon} \cdot \vec{r} \lvert i \rangle \rvert^2 \ .$$

$\hat{\epsilon}$ is the polarization vector of the light, $\vec{r}$ the dipole operator, and m_s denotes the projection of the final-state spin along some axis. The rotational symmetry of the gas phase is destroyed by the presence of the surface; as we have seen, the crystal field removes degeneracies present in the free atom, giving rise to adatom states of different energies which have a specific orientation and which (aside from $p_{1/2}$ states) are not spherically symmetric. Hence, we can expect at the outset that the observed angular distributions of electrons from these levels will differ from their gas-phase analogs, provided the levels can be energy re-

solved.

The initial adsorbate states $\lvert i \rangle$ in the presence of the crystal field have been found in Sec. II for the cases of interest here. For the final state $\lvert f \rangle$ we use the partial-wave expansion employed in nonrelativistic atomic calculations:

$$\lvert fm_s \rangle = 4\pi \sum_{lm} i^l e^{-i\delta_l} Y_{lm}^*(\hat{k}) Y_{lm}(\hat{r}) R_{\epsilon l}(r) \lvert m_s \rangle \ .$$

$$(9)$$

$\lvert f \rangle$ satisfies ingoing wave boundary conditions. δ_l is the lth-wave phase shift due to the hole potential, $\hat{k}$ the direction of the outgoing electron's momentum, and $R_{\epsilon l}(r)$ a continuum radial wave function which is a solution of the Schrödinger equation with the appropriate hole potential (ϵ the kinetic energy of the outgoing electron).

As Tables I–III and Eqs. (4) show, the initial states $\lvert i \rangle$ are all linear combinations of states such as

$$\lvert l'm'm_s' \rangle = R_{nl'j}(r) Y_{l'm'}(\Omega) \lvert m_s' \rangle \ .$$

With the help of Eq. (5) we find

$$\langle fm_s \lvert \hat{\epsilon} \cdot \vec{r} \lvert l'm'm_s' \rangle$$

$$= \frac{1}{\sqrt{2}} \delta_{m_s, m_s'} \sum_l \{\epsilon_x[-c^1(lm'+1, l'm')a(lm'+1) + c^1(lm'-1, l'm')a(lm'-1)]$$

$$+ i\epsilon_y[c^1(lm'+1, l'm')a(l'm'+1) + c^1(lm'-1, l'm')a(lm'-1)] + \sqrt{2}\ \epsilon_z[c^1(lm', l'm')a(lm')]\} \ ,$$

$$(10)$$

TABLE IV. Angular distributions $I_i(E_i) = \frac{1}{18}\pi\alpha\omega N_i\{A_1R_d^2 + A_2[2R_dR_s\cos(\delta_d - \delta_s)] + A_3R_s^2\}$ for p states in fourfold sites (atomic units). The crystal-field energies E_1, E_2, E_3 are those of Table I; $t \equiv \cos\theta$.

	Angular distributions	A_1	A_2	A_3
$p_{1/2}$:	$I_1(E_1)$	$-3t^2 + 5$	$3t^2 - 1$	2
$p_{3/2}$:	$I_2(E_2)$	$\frac{27}{2}t^4 - 18t^2 + \frac{15}{2}$	$\frac{3}{2}(3t^2 - 1)$	3
	$I_3(E_3)$	$-\frac{27}{2}t^4 + 12t^2 + \frac{5}{2}$	$\frac{1}{2}(3t^2 - 1)$	1

in which

$$a(lm) \equiv 4\pi(-i)^l R_l e^{i\delta_l} Y_{lm}(\hat{k}) \ , \tag{11}$$

$$R_l \equiv \int_0^\infty r^3 \, dr \, R_{nl'j}(r) R_{\epsilon l}(r) \ . \tag{12}$$

The sum on l in Eq. (10) is restricted to the values $l = l' \pm 1$ by the dipole selection rule. The matrix element $\langle fm_s|\hat{\epsilon} \cdot \vec{r}|i\rangle$ for a particular adatom state $|i\rangle$ is a sum of terms such as those given in Eq. (10).

To contrast the effect of different site geometries on the angular distributions and to compare the emission from p and d adatom states we specialize the examples of this section to unpolarized light at normal incidence ($\epsilon_z = 0$). The angular distribution for a state $|i\rangle$ is then the incoherent average of the intensities for x and y linearly polarized light, and the total distribution for a doubly degenerate crystal-field level involves the addition of the cross sections for the two (orthogonal) degenerate states corresponding to that level. Furthermore, since we are not concerned with the angular distribution of spin polarization in this work, the quantization axis for the final-state spin is immaterial; for simplicity we choose it to be the same as for the initial states, namely the z axis of Fig. 1. With this choice the differential cross section $I_i(E_i)$ for an adatom level distinguished by its energy E_i (and for normal incidence, unpolarized light) is[7]

$$I_i(E_i) = K(\omega) \sum_{\nu=1,2} (|\langle fm_s|x|i_\nu\rangle|^2 + |\langle fm_s|y|i_\nu\rangle|^2) \ . \tag{13}$$

$K(\omega)$ represents a group of factors dependent on the photon energy $\hbar\omega$ but independent of angular variables. Calculation of the angular distributions $I_i(E_i)$ is straightforward although algebraically tedious in some instances. In the results which follow all quantities are expressed in atomic units and the angular variables (θ, ϕ) specifying the direction of the photoelectron momentum are referred in the standard manner to the coordinate axes of Fig. 1.

A. p states in fourfold sites

Table IV presents results for this simplest case in the following form:

$$\begin{aligned} I_i(E_i) = \frac{1}{18}\pi\alpha\omega N_i \{ & A_1(\theta)R_d^2 \\ & + A_2(\theta)[2R_dR_s\cos(\delta_d - \delta_s)] \\ & + A_3R_s^2 \} \ . \end{aligned} \tag{14a}$$

R_s and R_d are the radial matrix elements of Eq. (12) for $l = 0$ and $l = 2$, respectively, and δ_s, δ_d the corresponding phase shifts; these quantities are to be evaluated for the kinetic energy ϵ appropriate to each crystal-field level. α is the fine-structure constant, and $N_i = 0$, 1, or 2 is the occupation number of the level. The distributions do not exhibit any azimuthal dependence because the initial-state charge densities do not.

B. p states in bridge sites

The angular distribution for the $p_{1/2}$ states is the same as that given in Table IV for the fourfold geometry, and the distributions for the $p_{3/2}$ states can be written

$$\begin{aligned} I_i(E_i) = \frac{1}{18}\pi\alpha\omega N_i \{ & A_1(\theta, \phi)R_d^2 \\ & + A_2(\theta, \phi)[2R_dR_s\cos(\delta_d - \delta_s)] \\ & + A_3R_s^2 \} \ . \end{aligned} \tag{14b}$$

These are listed in Table V, whose entries are for either x-bridge or y-bridge sites, the coefficient a_2 having opposite sign in the two instances. The twofold symmetry of the bridge sites is made apparent by the terms involving $\cos2\phi$, which result from the mixing of the free-atom states to conform to the site symmetry and the fact that $l = 2$ final states can be excited. Note that $I_3(E_3)$ is given by $I_2(E_3)$ with the replacements $a_1 \to a_2$, $a_2 \to -a_1$; this is obvious from the form of the initial-state wave functions in Table II. In the limit $a_1 \to 1$ $(a_2 \to 0)$ the initial states become identical to those of the previous subsection, and Table V results reduce to those of Table IV.

An interesting effect occurs if $p \to d$ transitions dominate the cross section $(R_s \to 0)$. The intensi-

TABLE V. Angular distributions $I_i(E_i) = \frac{1}{18}\pi\alpha\omega N_i\{A_1R_d^2 + A_2[2R_dR_s\cos(\delta_d - \delta_s)] + A_3R_s^2\}$ for $p_{3/2}$ states in x- or y-bridge sites (a.u.). The crystal-field energies E_2, E_3 and mixing coefficients a_1, a_2 are those of Table II; $t \equiv \cos\theta$.

Angular distributions	A_1	A_2	A_3
$I_2(E_2)$	$\frac{27}{2}t^4 - 18t^2 + \frac{15}{2}$ $-3a_2^2(9t^4 - 10t^2 + \frac{5}{3})$ $+3\sqrt{3}\,a_1a_2(1 - t^2)(3t^2 - 1)\cos2\phi$	$(\frac{3}{2} - a_2^2)(3t^2 - 1)$ $+3\sqrt{3}\,a_1a_2(1 - t^2)\cos2\phi$	$3 - 2a_2^2$
$I_3(E_3)$	$\frac{27}{2}t^4 - 18t^2 + \frac{15}{2}$ $-3a_1^2(9t^4 - 10t^2 + \frac{5}{3})$ $-3\sqrt{3}\,a_1a_2(1 - t^2)(3t^2 - 1)\cos2\phi$	$(\frac{3}{2} - a_1^2)(3t^2 - 1)$ $-3\sqrt{3}\,a_1a_2(1 - t^2)\cos2\phi$	$3 - 2a_1^2$

ties are then given by the A_1 components alone, and the coefficient of the cos2φ term in I_2 and I_3 reverses sign at the polar angle θ_{magic} $=\cos^{-1}(1/\sqrt{3})$, implying a 90° rotation of the intensity pattern maxima about the z axis as θ passes through θ_{magic}.

For an experimental situation in which the two kinds of bridge sites are equally occupied, the angular distributions in this model are given by the average of the x- and y-bridge results. Since the coefficient a_2 has opposite sign in the two cases, this means that the appropriate distributions are those of Table V with the cos2φ terms *omitted*.

C. d states in fourfold sites

In the dipole formulation p and f partial waves can be excited from d initial states. Cross sections for the d-electron crystal-field levels in the fourfold geometry can be expressed as

$$I_i(E_i) = \frac{3}{100}\pi\alpha\omega N_i\{A_1(\theta, \phi)R_f^2$$
$$+ A_2(\theta, \phi)[2R_fR_p\cos(\delta_f - \delta_p)]$$
$$+ A_3(\theta)R_p^2\}\,, \tag{15}$$

where R_f, R_p and δ_f, δ_p are radial matrix elements and phase shifts for $l = 3$ and $l = 1$, respectively, evaluated at suitable kinetic energies. Table VI presents the results of our calculations. The form of the wave functions for E_4 and E_5 in Table III shows that $I_5(E_5)$ is identical to $I_4(E_5)$ with $a_1 \rightarrow a_2$, $a_2 \rightarrow -a_1$.

The fourfold symmetry is clearly demonstrated by the dependence of I_4 and I_5 on the azimuthal angle ϕ. Gadzuk[8] has discussed this property for crystal-field d states in the absence of the spin-orbit interaction. He specifically considered the $d_{x^2-y^2}$ orbitals, which most closely correspond to the initial states of I_4 and I_5, and recognized a novel characteristic that prevails here as well and is analogous to the behavior we noted for p states

TABLE VI. Angular distributions $I_i(E_i) = \frac{3}{100}\pi\alpha\omega N_i\{A_1R_f^2 + A_2[2R_fR_p\cos(\delta_f - \delta_p)] + A_3R_p^2\}$ for d states in fourfold sites (a.u.). The crystal field energies $E_1, \ldots, E_5$ and mixing coefficients a_1, a_2 are given in Table III; $t \equiv \cos\theta$.

Angular distributions		A_1	A_2	A_3
$d_{3/2}$	$I_1(E_1)$	$15t^4 - 26t^2 + 13$	$-5t^4 + 9t^2 - 2$	$2(-3t^2 + 4)$
	$I_2(E_2)$	$-15t^4 + 18t^2 + 3$	$5t^4 + 3t^2 - 2$	$\frac{2}{3}(7t^2 + 2)$
$d_{5/2}$	$I_3(E_3)$	$\frac{1}{2}(-125t^6 + 155t^4 - 31t^2 + 9)$	$-5t^4 + 12t^2 - 3$	$2(t^2 + 1)$
	$I_4(E_4)$	$\frac{5}{4}(-25t^6 + 55t^4 - 43t^2 + 13)$ $+a_2^2(125t^6 - 215t^4 + 111t^2 - 13)$ $-\frac{5}{2}(5)^{1/2}a_1a_2(1 - t^2)^2(5t^2 - 1)\cos4\phi$	$\frac{5}{2}(1 - t^2)(5t^2 - 1)$ $+2a_2^2(15t^4 - 12t^2 + 1)$ $-5(5)^{1/2}a_1a_2(1 - t^2)^2\cos4\phi$	$10(1 - t^2)$ $+8a_2^2(2t^2 - 1)$
	$I_5(E)$	$\frac{5}{4}(-25t^6 + 55t^4 - 43t^2 + 13)$ $+a_1^2(125t^6 - 215t^4 + 111t^2 - 13)$ $+\frac{5}{2}(5)^{1/2}a_1a_2(1 - t^2)^2(5t^2 - 1)\cos4\phi$	$\frac{5}{2}(1 - t^2)(5t^2 - 1)$ $+2a_1^2(15t^4 - 12t^2 + 1)$ $+5(5)^{1/2}a_1a_2(1 - t^2)^2\cos4\phi$	$10(1 - t^2)$ $+8a_1^2(2t^2 - 1)$

in bridge sites. For kinetic energies great enough
so that the f-wave channel dominates [$R_p \to 0$ in Eq.
(15)], I_4 and I_5 are given by the A_1 terms alone,
and each is of the form [$f(\theta) + g(\theta) \cos 4\phi$]. As
Table VI indicates, the sign of $g(\theta)$ depends on that
of $(5\cos^2\theta - 1)$, which reverses sign as θ passes
through $\theta_{magic} = \cos^{-1}(1/\sqrt{5})$ and gives rise to a 45°
rotation about the z axis of the intensity distribu-
tion maxima.

D. Correspondence with gas-phase theory

In the gas phase the orientation of an atom is
completely random, and calculation of the photo-

ionization cross section involves a suitable angular
average to take this into account. Structural in-
formation is lost in the averaging process, and the
differential cross section in the dipole approxima-
tion assumes the simple form[9]

$$\frac{d\sigma}{d\Omega} = \frac{\sigma_l(\epsilon)}{4\pi}\,[1 - \tfrac{1}{2}\beta_l(\epsilon)P_2(\Theta)] \ . \tag{16}$$

Equation (16) is the nonrelativistic, single-parti-
cle result for a shell comprised of electrons with
orbital angular momentum l irradiated by unpolar-
ized light. Θ is the angle between the photon and
photoelectron momenta, $P_2(\Theta) \equiv \tfrac{1}{2}(3\cos^2\Theta - 1)$, and
the asymmetry parameter $\beta_l(\epsilon)$ is defined by

$$\beta_l(\epsilon) = \frac{l(l-1)R_{l-1}^2(\epsilon) + (l+1)(l+2)R_{l+1}^2(\epsilon) - 6l(l+1)R_{l-1}(\epsilon)R_{l+1}(\epsilon)\cos[\delta_{l+1}(\epsilon) - \delta_{l-1}(\epsilon)]}{(2l+1)[lR_{l-1}^2(\epsilon) + (l+1)R_{l+1}^2(\epsilon)]} \ , \tag{17}$$

where $\sigma_l(\epsilon)$ is the total cross section; in atomic
units it is

$$\sigma_l(\epsilon) = \tfrac{4}{3}\pi^2\alpha\omega[N_l/(2l+1)]$$
$$\times [lR_{l-1}^2(\epsilon) + (l+1)R_{l+1}^2(\epsilon)] \ , \tag{18}$$

where N_l is the occupation number of the shell.

Even in the presence of a crystal field the $p_{1/2}$
states are spherically symmetric, implying that
the cross section must be the same as for the gas
phase. It is easily verified that $I_1(E_1)$ of Table IV
can be rewritten to correspond precisely to Eq.
(16) with $l = 1$ (Θ is to be identified with θ in this
section).

A consistency check on the other results of Secs.
III A–III C can be made by observing that a half-filled
or filled spin-orbit subshell is spherically symme-
tric. Hence, if we assign the same occupation number
N_i (equal to 1 or 2) to each crystal-field level of a

given j and neglect the energy splitting (so that all
kinetic energies are equal), then the sum of the
intensities for these levels must reproduce the
cross section of Eq. (16). This is a consequence
of the fact that the crystal-field states used here
are simply orthonormal linear combinations of
free-atom spin-orbit states having the same j.

In particular, we find from either Table IV for
$p_{3/2}$ states in fourfold sites or from Table V for
$p_{3/2}$ states in bridge sites (noting that $a_1^2 + a_2^2 = 1$)
that

$$I_2(E) + I_3(E) = \tfrac{2}{9}\pi\alpha\omega N_i(R_s^2 + 2R_d^2)$$
$$\times [1 - \tfrac{1}{2}\beta_p(\epsilon)P_2(\Theta)] \ . \tag{19}$$

This corresponds to Eq. (16) with $l = 1$ and N_l
$= 2N_i$, $N_i = 2$ for a half-filled and $N_l = 4$ for a filled
$p_{3/2}$ subshell. Similarly, the distributions for d
states in fourfold sites (Table VI) satisfy

$$\left.\begin{array}{l}(j = \tfrac{3}{2})\ I_1(E) + I_2(E) \\ (j = \tfrac{5}{2})\ I_3(E) + I_4(E) + I_5(E)\end{array}\right\} = \tfrac{1}{30}(2j+1)\pi\alpha\omega N_i(2R_p^2 + 3R_f^2)[1 - \tfrac{1}{2}\beta_d(\epsilon)P_2(\Theta)] \ ; \tag{20}$$

that is, we recover Eq. (16) with $l = 2$ and N_l
$= [(2j+1)/2]N_i$ for the $d_{3/2}$ and $d_{5/2}$ levels separate-
ly. $\tfrac{1}{2}(2j+1)$ is the number of (doubly degenerate)
crystal-field levels.

IV. APPLICATION: Xe ON W(100)

Ultraviolet photoemission spectra obtained[10] for
xenon physisorbed on a tungsten (100) surface are
characterized by two peaks associated with emis-
sion from the Xe $5p_{1/2}$ and $5p_{3/2}$ levels. The dif-
ference between the clean tungsten spectrum and

the spectrum after exposure to 5 langmuirs (1 L
$= 10^{-6}$ Torr sec), $\sim 7 \times 10^{-4}$ Pa sec, of Xe is shown
in Fig. 2. The spin-orbit splitting of the two levels
and their intensity ratio agree closely with gas-
phase measurements,[11] while the $5p_{3/2}$ peak is
broadened by ~ 0.3 eV with respect to the $5p_{1/2}$.
Waclawski and the author have suggested[10] that the
broadened structure may be an unresolved doublet
which results from the splitting of the Xe $5p_{3/2}$
states in the crystal field of the tungsten surface.
Assuming fourfold sites and using the results of
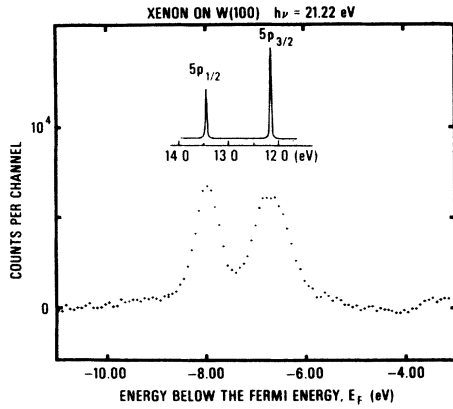the calculations detailed in Sec. II of this paper,

FIG. 2. Difference spectrum for Xe physisorbed on a W(100) surface (from Ref. 10). The inset is the photoelectron distribution for gaseous Xe (Ref. 11).

FIG. 4. Photoelectron spectra of Hg on W(100) for different polar angles θ (from Ref. 14).

they found that a point charge $Z \sim \frac{1}{2}|e|$ can produce a 0.3-eV separation of the $5p_{3/2}$ levels.

Unfortunately, no angle-resolved measurements have been carried out for the Xe-W(100) system. We wish to point out that the simple model for the angular distributions analyzed here leads to an interesting prediction for the Xe crystal-field states. Employing nonrelativistic dipole matrix elements and phase shifts provided by Manson[12] for xenon $5p$ electrons at the appropriate kinetic energy,[13] we have calculated the ratio I_2/I_3 of the distributions given in Table IV for $p_{3/2}$ states in the fourfold geometry (normal incidence, unpolarized light). Figure 3 presents a graph of this ratio as a function of polar angle θ. I_2/I_3 varies by an order of magnitude, suggesting that an angular measurement with sufficient energy resolution may at least reveal anisotropy in the Xe $5p_{3/2}$ structure as a function of θ. Such an experiment could provide further information regarding the validity of the crystal-field hypothesis. (For equally occupied x- and y-bridge sites the ratio I_2/I_3 is not
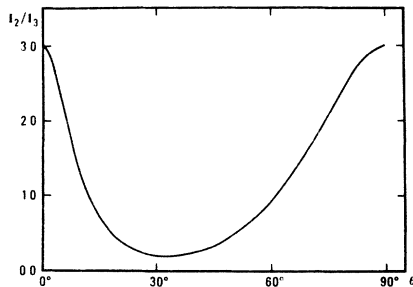

FIG. 3. Ratio I_2/I_3 of the $p_{3/2}$ angular distributions for Xe absorbed on a W(100) surface as a function of polar angle θ.
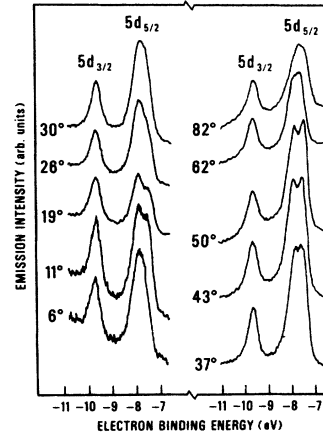
perceptibly different from that presented in Fig. 3 for the fourfold geometry.)

V. CALCULATIONS FOR Hg ON W(100) AND COMPARISON WITH EXPERIMENT

Egelhoff, Perry, and Linnett (EPL) have investigated[14] mercury adsorbed on a tungsten (100) surface by means of ultraviolet photoemission. Spectra were obtained over a range of polar angles θ in a spectrometer having the angle between the photon beam and detector fixed at 90°; $k_{\parallel}$, the component of photoelectron momentum parallel to the surface, was in the [11] direction. Of particular interest to us here is the structure of the spectra in the region of the Hg $5d$ peaks; the distributions measured by EPL are shown in Fig. 4. In this section we explore the possibility that the crystal-field mechanism may qualitatively account for some of the observed features.

A. Crystal-field splittings

We first use the results of Sec. II C to estimate the splitting of the Hg $5d$ states, assuming that fourfold sites are occupied. We find $h = 1.9$ Å, $R_1 = 2.9$ Å, and $R_2 = 3.5$ Å through the use of 3.16 Å for the W lattice constant and "hardball" radii of 1.4 and 1.6 Å for W and Hg, respectively. Relativistic Hartree-Fock calculations[15] for mercury yield $\langle r^2 \rangle_{3/2} = 0.68$ Å^2, $\langle r^2 \rangle_{5/2} = 0.75$ Å^2, and $\langle r^4 \rangle_{5/2} = 1.06$ Å^4 for the $5d$ subshells. With the assumption that $Z > 0$, this information leads to the level ordering displayed in Fig. 5 with the separations $E_1 - E_2 = 0.17Z$ (eV), $E_5 - E_3 = 0.06Z$ (eV), and $E_4 - E_3 = 0.24Z$ (eV). For a given Z the E_4 level is most distant from its crystal-field companions.

In Fig. 4 two peaks are apparent in the $5d_{5/2}$ structure for $\theta = 11°$, 19°, and 37°–50°; their sep-
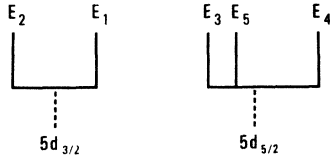
FIG. 5. Ordering of the $5d$ crystal-field levels on a (100) surface assuming $Z > 0$. Energy increases on the right-hand side.

aration is constant at approximately 0.37 eV. If we identify the peak of lower binding energy (right-most in the spectra) with E_4 and the other peak with an unresolved combination of the E_3 and E_5 levels, then $Z \sim 1.8|e|$ is required to give a 0.37-eV energy difference. With this value we obtain $E_1 - E_2 = 0.30$ eV and $E_5 - E_3 = 0.10$ eV. Noting the stated 0.2-eV resolution of EPLs energy analyzer we would thus expect E_5 and E_3 to be unresolved; on the other hand, E_1 and E_2 might be thought dis-tinguishable, but no clear indication of this is to be seen in $5d_{3/2}$ structures of Fig. 4. The ratio of the full widths at half maximum for the $d_{5/2}$ to $d_{3/2}$ levels is about 1.8 for each of the observed spectra, and this value is in fair agreement with the ratio $(E_4 - E_3)/(E_1 - E_2) = 1.4$ of the total extents of the $5d_{5/2}$ and $5d_{3/2}$ crystal-field energies.

B. Angular distributions

To find the distributions appropriate to EPLs work in our simple model we observe that the po-larization vectors for s- and p-polarized light may be chosen to be $\hat{\epsilon}_s = \hat{y}$ and $\hat{\epsilon}_p = \hat{x}\sin\theta + \hat{z}\cos\theta$ in the coordinate system of Sec. II. For unpolar-ized light we must then calculate

$$I_i(E_i) = K(\omega) \sum_{m_s; \nu = 1, 2} \left(|\langle fm_s | y | i_\nu \rangle|^2 \right.$$
$$\left. + |\langle fm_s | x \sin\theta + z \cos\theta | i_\nu \rangle|^2 \right),$$

(21)

which is the analog of Eq. (13). This is routinely accomplished with the initial states $|i\rangle$ given in Table III, and the results are listed in Table VII. $k_\parallel$ is in the x direction for EPLs experiment, and, accordingly, the table entries are for $\phi = 0$; al-though we do not include results for arbitrary ϕ, the distributions have an azimuthal dependence which is more complex than those derived in Sec. III C for normal incidence light. Since the angle between the photon and photoelectron momenta is $90°$ in this case, the correspondences with the gas-phase results should be given by Eq. (20) with $\Theta = \frac{1}{2}\pi$ $[P_2(\Theta) = -\frac{1}{2}]$, and the intensities of Table VII satisfy those conditions.

We have evaluated the results of Table VII by again employing dipole matrix elements and phase shifts provided by Manson[12]; the distributions are presented[16] in Fig. 6. Although the intensities I_1, I_2 calculated for the $d_{3/2}$ levels differ by as much as a factor of 9 over the range of polar angles, no clear anisotropy is evident in the experimental spectra (Fig. 4); perhaps insufficient energy resol-ution is responsible. The most prominent aspect of Fig. 6 is that the distribution I_4, which corre-sponds to the crystal-field level most separated from its neighbors, grows rapidly with increasing θ while I_3 and I_5, its $d_{5/2}$ companions, do not. With the input parameters of Sec. V A $a_1 \sim 1$ $(a_2 \sim 0)$; hence, the E_4 level is almost entirely $|\frac{5}{2} \pm \frac{5}{2}\rangle$ (see Table III). The charge density of $|\frac{5}{2} \pm \frac{5}{2}\rangle$ rises continuously from zero at $\theta = 0°$ to a maximum at $\theta = 90°$, and this is responsible for the increase of

TABLE VII. Polar angle distributions $I_i(E_i) = \frac{3}{100}\pi\alpha\omega N_i\{A_1 R_f^2 + A_2[2R_f R_p \cos(\delta_f - \delta_p)] + A_3 R_p^2\}$ for d states in fourfold sites (a.u.). Photon and photoelectron momenta are perpendicular in the $\phi = 0$ plane. The crystal-field energies $E_1, \ldots, E_5$ and mixing coefficients a_1, a_2 are those of Table III; $t \equiv \cos\theta$.

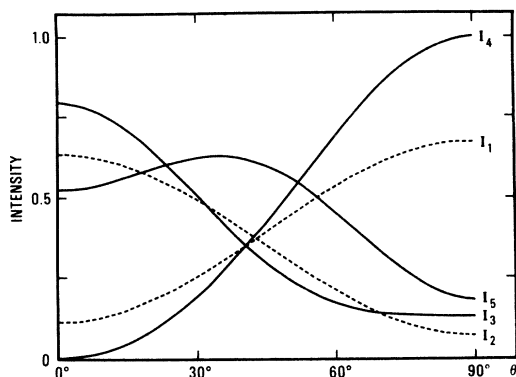| Angular distributions		A_1	A_2	A_3
$d_{3/2}$	$I_1(E_1)$	$-12t^2 + 13$	$3t^2 - 2$	$-7t^2 + 8$
	$I_2(E_2)$	$12t^2 + 3$	$-3t^2 - 2$	$7t^2 + \frac{4}{3}$
$d_{5/2}$	$I_3(E_3)$	$\frac{45}{2}t^4 - 7t^2 + \frac{9}{2}$	$-15t^4 + 8t^2 - 3$	$2(5t^4 - t^2 + 1)$
	$I_4(E_4)$	$\frac{45}{4}t^4 - \frac{55}{2}t^2 + \frac{65}{4}$	$-\frac{15}{2}t^4 + 10t^2 - \frac{5}{2}$	$5(t^4 - 3t^2 + 2)$
		$+ a_2^2(-45t^4 + 62t^2 - 13)$	$+ 2a_2^2(15t^4 - 14t^2 + 1)$	$+ 4a_2^2(-5t^4 + 8t^2 - 2)$
		$+ (5)^{1/2}a_1a_2(\frac{9}{2}t^4 - 7t^2 + \frac{5}{2})$	$-(5)^{1/2}a_1a_2(3t^4 - 8t^2 + 5)$	$-2(5)^{1/2}a_1a_2t^2(1 - t^2)$
	$I_5(E_5)$	$\frac{45}{4}t^4 - \frac{55}{2}t^2 + \frac{65}{4}$	$-\frac{15}{2}t^4 + 10t^2 - \frac{5}{2}$	$5(t^4 - 3t^2 + 2)$
		$+ a_1^2(-45t^4 + 62t^2 - 13)$	$+ 2a_1^2(15t^4 - 14t^2 + 1)$	$+ 4a_1^2(-5t^4 + 8t^2 - 2)$
		$-(5)^{1/2}a_1a_2(\frac{9}{2}t^4 - 7t^2 + \frac{5}{2})$	$+(5)^{1/2}a_1a_2(3t^4 - 18t^2 + 5)$	$+2(5)^{1/2}a_1a_2t^2(1 - t^2)$

FIG. 6. Angular distributions of Table VII evaluated for the Hg-W(100) system as a function of polar angle θ. (A common angle-independent factor has been omitted from each distribution.)

emission from the E_4 level with larger θ. The measured spectra do indeed show the peak of lowest binding energy to gain intensity with larger polar angle, lending additional credence to its identification with the E_4 level. The ratio $(I_3+I_4+I_5)/(I_1+I_2)$ of the calculated $d_{5/2}$ and $d_{3/2}$ total intensities is ~1.8 for all θ, but without more detailed knowledge of background effects in the experimental distributions, especially their variation with θ, it is difficult to compare the calculated and experimental ratios. At any rate, there is some qualitative similarity between the results of the model and experiment.

VI. REMARKS

We have shown that the angular distributions of electrons emitted from a physisorbed atom can assume forms quite distinct from those of the same atom in the gas phase. This stems principally from the orientation of the adsorbate on the surface. The crystal field introduced here provides an interaction of appropriate symmetry which removes some free-atom degeneracies and produces states separated in energy whose associated charge densities are not spherically symmetric. The distributions we have derived reduce to the gas-phase analogs in suitable limits, providing a useful consistency check as well as explicitly verifying the loss of orientational information in the gas phase. Although we have confined our attention to metals because of the availability of experimental results for metal substrates, the distributions for atoms physisorbed on a semiconductor or ionic solid can be obtained within this model by modification of the crystal

potential; however, the form of the angular distributions for the site symmetries studied here will remain unchanged.

Our straightforward atomic treatment neglects any bonding between adatom and substrate orbitals. For physisorbed systems this approximation is a reasonable one, especially for the mercury $5d$ states specifically considered in this paper since they are inside the spatially more extended $6s$ electrons. Appreciable bonding between adatom p and substrate d states, for instance, would give rise to an azimuthal dependence of the emission in the fourfold geometry for normal incidence, unpolarized light (as Gadzuk has noted[1]) which the adsorbate p states alone cannot generate.

We have also ignored lattice backscattering effects of the kind discussed[2] by Liebsch. Assessment of the influence of these effects must await measurements of the azimuthal dependence of the emission. The qualitative agreement between our results and the mercury and xenon measurements gives preliminary support for the crystal-field mechanism, but more experiments are certainly necessary before a definitive conclusion can be reached.

Finally, we note that interactions having the same symmetry as the crystal field may lead to similar energy splittings even though their origins are different. The screening of the hole left behind by the photoejected electron is such a possibility. The interaction between the positive hole and the substrate electronic charge distribution has the same symmetry as the crystal field of our set of positive point charges interacting with an adsorbate electron in its initial state, and inequivalent screening of different adsorbate orbitals may contribute to the observed structures. Matthew and Devey have suggested[17] that a considerable part of the broadening of the $5p_{3/2}$ peak in the Xe-W(100) spectra results from such an effect; however, their estimate is predicted upon a classical image force argument and probably represents an upper limit for the possible energy splitting. Our determination of Z by fitting to experiment includes all effects of the same symmetry, but further analysis is required to ascertain the individual contributions.

ACKNOWLEDGMENTS

*Present address: Physics Department, Brookhaven National Laboratory, Upton, New York 11973.

†Work supported by NRC-NBS Postdoctoral Research Associateship.

[1] J. W. Gadzuk, Solid State Commun. 15, 1011 (1974); Phys. Rev. B 10, 5030 (1974).

[2] Ansgar Liebsch, Phys. Rev. Lett. 32, 1203 (1974); Phys. Rev. B 13, 544 (1976).

[3] P. V. S. Rao and J. T. Waber [Surf. Sci. 28, 299 (1971)] have previously treated crystal-field effects using this configuration. The spin-orbit interaction was not included in their analysis, however, and for Xe and Hg systems we consider in this work the atomic spin-orbit splitting is large compared to the crystal-field splittings.

[4] This assumption can only affect the magnitude of the splittings for the fourfold case, in which the point charge in the second plane should probably be assigned a smaller value than that of the point charges in the first plane.

[5] See, for example, E. U. Condon and G. H. Shortley, The Theory of Atomic Spectra (Cambridge University, Cambridge, 1967), p. 123.

[6] Reference 5, pp. 178–179.

[7] We have neglected an explicit sum over m_s in Eq. (13) since for normal incidence, unpolarized light the right-hand side is the same for $|m_s\rangle = |\uparrow\rangle$ and $|m_s\rangle = |\downarrow\rangle$.

[8] J. W. Gadzuk, Phys. Rev. B 12, 5608 (1975).

[9] D. J. Kennedy and S. T. Manson, Phys. Rev. A 5, 227

(1972).

[10] B. J. Waclawski and J. F. Herbst, Phys. Rev. Lett. 35, 1594 (1975).

[11] D. W. Turner, Molecular Photoelectron Spectroscopy (Wiley, New York, 1970), p. 42.

[12] S. T. Manson (private communication).

[13] From Ref. 10 the center of the $5p_{3/2}$ structure is 6.8 eV below the Fermi level. This value together with the photon energy of 21.2 eV and a work function of 3.7 eV for the exposed surface implies a 10.7-eV photoelectron kinetic energy. The variation of the dipole matrix elements and phase shifts on the 0.3-eV scale of the broadening is negligible, and so we have used the same values in calculating both I_2 and I_3.

[14] W. F. Egelhoff, Jr., D. L. Perry, and J. W. Linnett, Surf. Sci. 54, 670 (1976).

[15] R. E. Watson and I. Lindgren (private communication).

[16] The results of Fig. 6 incorporate matrix elements and phase shifts evaluated at the 7.1- and 9.1-eV kinetic energies corresponding to the centroids of the observed $5d_{3/2}$ and $5d_{5/2}$ structures, respectively ($\hbar\omega = 21.2$ eV; the work function is 4.6 eV for the mercury-exposed surface); variation of these quantities with the smaller crystal-field splittings is unimportant. With this slight simplification the total $d_{3/2}$ intensity ($I_1 + I_2$) and total $d_{5/2}$ intensity ($I_3 + I_4 + I_5$) are θ-independent constants.

[17] J. A. D. Matthew and M. G. Devey, J. Phys. C 9, L413 (1976).